



Title	4α linear-chain state produced by $9\text{Be} + 9\text{Be}$ collisions
Author(s)	Baba, Tomoyuki; Taniguchi, Yasutaka; Kimura, Masaaki
Citation	Physical Review C, 105(6), L061301 https://doi.org/10.1103/PhysRevC.105.L061301
Issue Date	2022-06-08
Doc URL	https://hdl.handle.net/2115/86335
Rights	©2022 American Physical Society
Type	journal article
File Information	PhysRevC.105(6)_L061301.pdf



4α linear-chain state produced by ${}^9\text{Be} + {}^9\text{Be}$ collisionsTomoyuki Baba¹, Yasutaka Taniguchi^{2,3}, and Masaaki Kimura^{4,5,6,3}¹*Kitami Institute of Technology, 090-8507 Kitami, Japan*²*Department of Information Engineering, National Institute of Technology (KOSEN), Kagawa College, 769-1192 Mitoyo, Japan*³*Research Center for Nuclear Physics (RCNP), Osaka University, 567-0047 Ibaraki, Japan*⁴*Department of Physics, Hokkaido University, 060-0810 Sapporo, Japan*⁵*RIKEN Nishina Center, 351-0198 Wako, Japan*⁶*Reaction Nuclear Data Centre (JCPRG), Hokkaido University, 060-0810 Sapporo, Japan*

(Received 14 December 2021; revised 27 April 2022; accepted 23 May 2022; published 8 June 2022)

The linear-chain (LC) structure provides significant insights into quantum many-body systems with geometric configurations. In this study, $4\alpha + 2n$ LC was assessed in ${}^{18}\text{O}$. The excitation energies, moment of inertia, and α - and ${}^9\text{Be}$ -decay widths of the LC states were predicted using antisymmetrized molecular dynamics. We predict that there are two 4α LC bands, $K^\pi = 0^+$ and $K^\pi = 3^-$, which exhibit different decay properties. We demonstrate that the $K^\pi = 3^-$ LC states can be verified by the head-on ${}^9\text{Be} + {}^9\text{Be}$ collision experiments because their states exhibited large decay widths in the ${}^9\text{Be} + {}^9\text{Be}$ channel.

DOI: [10.1103/PhysRevC.105.L061301](https://doi.org/10.1103/PhysRevC.105.L061301)

Introduction. Nuclear clustering has many similarities with molecules. For instance, extra neutrons surrounding α -particles behave glue-like, analogous to the covalent electrons of atomic molecules such as beryllium ($2\alpha + xn$) [1–7], carbon ($3\alpha + xn$) [8], and heavier-mass isotopes [9–11]. In carbon isotopes ($3\alpha + xn$), it is expected that the extremely deformed states which have the intrinsic structure of three linearly aligned α particles, called the linear-chain (LC) structure, will be stabilized by the assistance of the glue-like covalent neutrons. Recent experimental [12–16] and theoretical [17–22] studies have identified LC states in ${}^{14}\text{C}(3\alpha + 2n)$, and researches on ${}^{16}\text{C}(3\alpha + 4n)$ have also been reported [23–25].

A longstanding open question is how many α particles can compose an LC structure. Unlike the 3α LCs, LCs containing four or more α particles have not been experimentally confirmed. ${}^A\text{Be} + {}^A\text{Be}$ resonant scattering can be a natural way to produce the 4α LC state in oxygen isotopes. Although the formation of the 4α LC in ${}^{16}\text{O}$ has been predicted by several theoretical studies [26–31], ${}^8\text{Be}$ is an unbound nucleus; therefore, its existence from the ${}^8\text{Be} + {}^8\text{Be}$ reaction is not easy. Given that ${}^9\text{Be}$ is the only stable Be isotope, ${}^9\text{Be} + {}^9\text{Be}$ scattering is the most feasible way to confirm the $4\alpha + 2n$ LC. Therefore, in this study, the excited states of ${}^{18}\text{O}$ were studied to identify a candidate $4\alpha + 2n$ LC.

Linear chain produced by ${}^9\text{Be} + {}^9\text{Be}$ collision. Let us consider the 4α LC configurations that will be produced by the head-on ${}^9\text{Be} + {}^9\text{Be}$ collisions. For simplicity, we approximate the ground state of ${}^9\text{Be}(3/2^-)$ as an $\alpha + \alpha + n$ system with a valence neutron occupying the $p_{3/2}$ orbit with $j_z = \pm 3/2$. As illustrated in Fig. 1, there are two ways to linearly align two ${}^9\text{Be}$, which yield different valence neutron configurations: (a) the antiparallel and (b) the parallel alignments with respect

to the j_z of the valence neutrons. The antiparallel alignment yields the intrinsic state with $K = 0$, where K denotes the z component of the intrinsic angular momentum and is equal to the sum of the j_z of valence neutrons. Because this configuration is an admixture of positive- and negative-parity states, we expect that it leads to a pair of rotational bands: $J^\pi = 0^+, 2^+, 4^+, \dots$ and $1^-, 3^-, 5^-, \dots$ bands. Indeed, we obtained both the bands in this study. However, we focus only on the $J^\pi = 0^+, 2^+, 4^+, \dots$ band, because the negative-parity bands are located at higher energies than the positive-parity band.

Parallel alignment [Fig. 1(b)] yields an intrinsic state with $K = 3$. The parity of this configuration is uniquely determined as negative for the following reasons. The spin wave function is symmetric ($S = 1$), as both neutron spins are aligned to $s_z = 1/2$. Because the isospin wave function is also symmetric, the spatial wave function must be asymmetric with respect to the exchange of two valence neutrons (parity transformation). Thus, this configuration forms a $J^\pi = 3^-, 4^-, 5^-, \dots$ band. Briefly, the antiparallel alignment yields a pair of positive- and negative-parity bands with $K = 0$, whereas the parallel alignment yields a negative-parity band with $K = 3$.

Calculated properties of the linear-chain states. To describe the LC states, we use antisymmetrized molecular dynamics (AMD). The Hamiltonian with the Gogny D1S nucleon-nucleon interaction is applied [32]. The AMD wave function Ψ_{AMD}^π is a parity-projected Slater determinant of single-particle wave packets,

$$\Psi_{\text{AMD}}^\pi = \hat{P}^\pi \Psi_{\text{AMD}} = \hat{P}^\pi \mathcal{A}\{\psi_1, \psi_2, \dots, \psi_A\}. \quad (1)$$

Here, \hat{P}^π is the parity-projection operator, and ψ_i is the single-particle wave packet, which is a direct product of the deformed

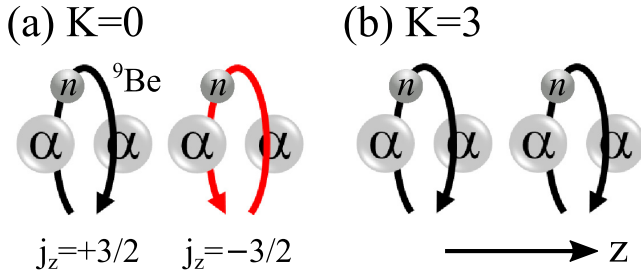


FIG. 1. Schematic illustration of the 4α LCs constructed by (a) antiparallel and (b) parallel alignments with respect to the j_z of the valence neutrons in ${}^9\text{Be}$. The black arrows indicate $j_z = +3/2$ orbit of the valence neutron, while the red arrow indicates $j_z = -3/2$.

Gaussian for the spatial part, spin (χ_i), and isospin (ξ_i) parts [33],

$$\phi_i(\mathbf{r}) = \prod_{\sigma=x,y,z} \exp\left\{-v_\sigma\left(r_\sigma - \frac{Z_{i\sigma}}{\sqrt{v_\sigma}}\right)^2\right\} \otimes \chi_i \otimes \xi_i,$$

$$\chi_i = a_i\chi_\uparrow + b_i\chi_\downarrow, \quad \xi_i = \text{proton or neutron.} \quad (2)$$

The centroids of the Gaussian wave packets \mathbf{Z}_i ; directions of nucleon spin a_i and b_i ; and width parameter v_σ are variables determined using the frictional cooling method [34]. In this study, we imposed a constraint on the quadrupole deformation parameter, β , to describe an extremely deformed 4α LC. After variational calculation, the eigenstate of the total angular momentum, J , is projected. We apply the generator coordinate method [35] by employing the quadrupole deformation parameter, β , as the generator coordinate.

In our previous work [36], we showed that AMD plausibly describes the low-lying states of ${}^{18}\text{O}$. The binding energy of ${}^{18}\text{O}$ was calculated as 139.97 MeV, whereas the observed value was 139.81 MeV. The low-lying excited states, including the ${}^{14}\text{C} + {}^4\text{He}$ cluster states, were also reasonably described. Therefore, we expect that AMD can precisely describe the higher-lying states of ${}^{18}\text{O}$.

It is noteworthy that the present calculation does not assume a prior LC configuration. In fact, we obtained many excited states with various cluster and noncluster states. Among these excited states, we assign two rational bands as the LC candidates shown in Fig. 2: a positive-parity band built on the 0^+ state followed by the 2^+ , 4^+ , \dots states, and a negative-parity band built on the 3^- state followed by 4^- , 5^- , \dots states. The spin-parity of these bands is consistent with that expected from the head-on ${}^9\text{Be} + {}^9\text{Be}$ configurations discussed above. This assignment is uniquely determined because of rather large $B(E2)$ strengths listed in Table I. In addition, the member states of each band dominantly have the same intrinsic structure, respectively. All the positive-parity band members have a large overlap with the intrinsic wave function shown in Fig. 3(a). Its proton density distribution shows a linear alignment of four α particles, and the two valence neutrons occupy negative-parity orbits with $j_z = \pm 3/2$. This intrinsic structure is approximately an antiparallel configuration, as shown in Fig. 1(a). However, in contrast to Fig. 1(a), the two valence neutrons are localized around two

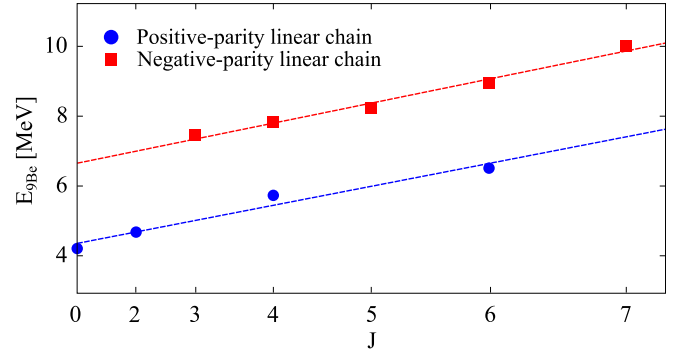


FIG. 2. Calculated energies above the ${}^9\text{Be} + {}^9\text{Be}$ threshold of the LC states as functions of angular momenta. The energy is relative to 23.64 MeV.

α particles at the center because of the attraction between valence neutrons and the absence of Pauli exclusion. Therefore, the entire system forms an $\alpha + {}^{10}\text{Be} + \alpha$ -like structure.

The intrinsic state of the negative-parity band is shown in Fig. 3(b1) and (b2). The proton density distribution indicates that this band also has a 4α LC core. One valence neutron occupies the negative-parity orbit with $j_z = 3/2$ [Fig. 3(b1)], and the other occupies the positive-parity orbit with $j_z = 3/2$ [Fig. 3(b2)]. These single-particle orbits can be understood as linear combinations of the $p_{3/2}$ orbits of the two ${}^9\text{Be}$. Let us denote the $p_{3/2}$ ($j_z = 3/2$) orbit of the left (right) side ${}^9\text{Be}$ as φ_L (φ_R), which is schematically illustrated by black arrows in Fig. 1(b). The single-particle orbits are then represented as

$$\varphi_\pm = \frac{1}{\sqrt{2}}(\varphi_L \pm \varphi_R). \quad (3)$$

They generate an orthogonalized pair of negative- and positive-parity orbits with $j_z = 3/2$, which correspond to Fig. 3(b1) and (b2), respectively. This intrinsic state corresponds to the parallel configuration shown in Fig. 1. In contrast to the antiparallel configuration, the two valence neutrons are located separately on the left Be and right Be because of the Pauli principle, which results from their parallel spin. We found that only these two bands have a structure corresponding to the head-on ${}^9\text{Be} + {}^9\text{Be}$ collision in the vicinity of the energies near the ${}^9\text{Be} + {}^9\text{Be}$ threshold. Since the pure head-on collision cannot be experimentally realized because of the angular momentum projection effect, the production probability of the LC configuration is suppressed. However,

TABLE I. Calculated $B(E2; J_i \rightarrow J_f)$ strengths for the $K^\pi = 0^+$ and $K^\pi = 3^-$ bands. The unit is $e^2\text{fm}^4$.

band	$J_i \rightarrow J_f$	$B(E2; J_i \rightarrow J_f)$
$K^\pi = 0^+$	$2^+ \rightarrow 0^+$	1072
	$4^+ \rightarrow 2^+$	1418
	$6^+ \rightarrow 4^+$	1692
$K^\pi = 3^-$	$4^- \rightarrow 3^-$	734
	$5^- \rightarrow 4^-$	546
	$6^- \rightarrow 5^-$	983
	$7^- \rightarrow 6^-$	807

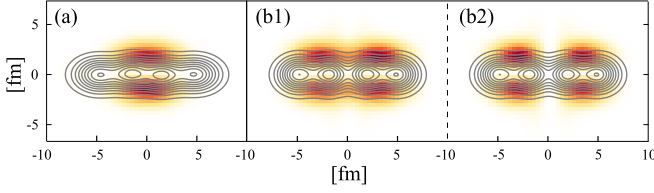


FIG. 3. Density distributions of the intrinsic states of the LC bands. The contour lines show the proton density distributions, and the color plots show the valence neutron orbits. (a) shows the intrinsic state of the positive-parity band, in which two valence neutrons occupy negative-parity orbits with $j_z = \pm 3/2$. (b1) and (b2) show the intrinsic state of the negative-parity band, in which a valence neutron occupies the negative-parity orbit with $j_z = 3/2$ (b1) and the other occupies the positive-parity orbit with $j_z = 3/2$ (b2).

the experimental ${}^9\text{Be} + {}^9\text{Be}$ collision is still a promising way to produce the LC states discussed later.

These two bands have strongly deformed intrinsic shapes that are compatible with a 4 α LC. The quadrupole deformation parameters of the positive- and negative-parity intrinsic states are equal to $\beta = 1.34$. Consequently, they have an enormous moment of inertia as large as $\hbar/2\mathfrak{I} = 55$ keV for the positive-parity band and 58 keV for the negative-parity band. These values are larger than that estimated for the rigid rotor, $\hbar/2\mathfrak{I} = 85$ keV, as follows. The classical moment of inertia of the prolate spheroid with 2 : 1, 3 : 1, and 4 : 1 deformations satisfies the following relation:

$$\mathfrak{I}_{2:1} : \mathfrak{I}_{3:1} : \mathfrak{I}_{4:1} = 5 : 15 : 34. \quad (4)$$

Because the moment of inertia of the 2 α and 3 α LCs are measured as $\hbar/2\mathfrak{I} = 590$ keV (2 $\alpha + 2n$) [37] and $\hbar/2\mathfrak{I} = 190$ keV in (3 $\alpha + 2n$) [15], respectively, the moment of inertia of 4 α LC is estimated as $\hbar/2\mathfrak{I} = 85$ keV.

Decay properties of the linear-chain states. To better understand the difference between the two LC bands, we discuss their α - and ${}^9\text{Be}$ -decay properties. Neutron emission channels are also open. However, in the present framework, it requires much computational cost to calculate their widths because of compound states. The calculated excitation energies, partial α -decay widths, and dimensionless reduced widths are listed in Table II. A dimensionless reduced width $\theta_l^2(a)$ is defined by

the ratio of the reduced width to the Wigner limit as follows:

$$\theta_l^2(a) = \frac{a}{3} |a y_l(a)|^2, \quad (5)$$

where $y_l(a)$ is the reduced width amplitude,

$$y_l(r) = \sqrt{\frac{A!}{A_{C1}! A_{C2}!}} \langle \phi_{C1} [\phi_{C2} Y_{l0}(\hat{r})]_{J^\pi M} | \Psi_{Mn}^{J^\pi} \rangle. \quad (6)$$

In the $\alpha + {}^{14}\text{C}$ channel, the daughter nucleus ${}^{14}\text{C}$ is assumed to be the 0^+ and 2^+ states of the 3 α LC states of ${}^{14}\text{C}$ reported previously in literature [19]. The reduced width in $\alpha + {}^{14}\text{C}(\text{g.s.})$ is almost zero because of the extreme deformation of the 4 α LC. The α -decay properties are different for the $K^\pi = 0^+$ and $K^\pi = 3^-$ LCs. The $K^\pi = 0^+$ LC states have very large α -decay widths in the LC states of ${}^{14}\text{C}$. Particularly, the widths of the $\alpha + {}^{14}\text{C}(2^+; \text{LC})$ channel are large because of the strong angular correlation between the linearly aligned α particles. This is in contrast to the Hoyle state, where α particles are weakly bound with $l = 0$; hence, the ${}^8\text{Be}(0_1^+)$ component dominates [38]. The large reduced width amplitude for $J^\pi = 0^+, 2^+, \dots$ is a significant LC structure feature. As the ${}^{14}\text{C}$ orientation is fixed, it does not become an eigenstate but a mixed state of angular momentum. A similar character has also been observed for the 3 α LC of carbon isotopes [19,23,26]. The $K^\pi = 3^-$ LC states have almost zero α -decay widths in the LC of ${}^{14}\text{C}$. It is clear that the both valence neutrons in the LC states of ${}^{14}\text{C}$ have negative parity; they are orthogonal to the LC of ${}^{18}\text{O}$, with the positive- and negative-parity valence neutrons shown in Fig. 3(b). Additionally, no negative-parity 3 α LC states of ${}^{14}\text{C}$ with the positive- and negative-parity valence neutrons are found [19]. Therefore, in the present calculation, the $K^\pi = 3^-$ LC states do not decay to any $\alpha + {}^{14}\text{C}$ channels.

Partial ${}^9\text{Be}$ -decay widths and dimensionless reduced widths are listed in Table III. Angular momentum projection was performed for both ${}^9\text{Be}$ while calculating the decay widths. The ${}^9\text{Be}$ in the developed LC structure has a mixed angular momentum. Therefore, the LC states branch into various channels, such as ${}^9\text{Be}(3/2^-) + {}^9\text{Be}(3/2^-)$ and ${}^9\text{Be}(3/2^-) + {}^9\text{Be}(5/2^-)$. We consider only these two channels, where ${}^9\text{Be}(3/2^-)$ and ${}^9\text{Be}(5/2^-)$ are the ground and excited states of ${}^9\text{Be}$, respectively. The characteristics of the decay widths are different for $K^\pi = 0^+$ and $K^\pi = 3^-$ LCs. The $K^\pi = 0^+$

TABLE II. Excitation energies, energies above ${}^9\text{Be} + {}^9\text{Be}$ threshold, partial α -decay widths, and dimensionless reduced widths of the 4 α LC states. ${}^{14}\text{C}$ has been assumed to be the 0^+ and 2^+ states of the LC band. The channel radius is 7.0 fm.

J^π	E_x [MeV]	E_{Be} [MeV]	$\Gamma_\alpha(0^+; \text{LC})$ [keV]	$\theta_\alpha^2(0^+; \text{LC}) [\times 10^{-2}]$	$\Gamma_\alpha(2^+; \text{LC})$ [keV]	$\theta_\alpha^2(2^+; \text{LC}) [\times 10^{-2}]$
0^+	27.85	4.21	382	8.21	1136	31.8
2^+	28.32	4.68	346	7.70	1044	13.4 ($l = 4$)
4^+	29.37	5.73	288	3.51	918	5.37 ($l = 2$)
6^+	30.16	6.51	160	5.39	572	10.2 ($l = 4$)
3^-	31.09	7.45	0	0.00	0	0.00
4^-	31.46	7.82	0	0.00	0	0.00
5^-	31.86	8.22	0	0.00	0	0.00
6^-	32.58	8.95	0	0.00	0	0.00
7^-	33.68	10.0	0	0.00	0	0.00

TABLE III. Partial ${}^9\text{Be}$ -decay widths and dimensionless reduced widths of the 4α LC states. ${}^9\text{Be}(3/2^-) + {}^9\text{Be}(3/2^-)$ and ${}^9\text{Be}(3/2^-) + {}^9\text{Be}(5/2^-)$ are assumed. The channel radius is 7.0 fm.

J^π	E_x [MeV]	E_{Be} [MeV]	$\Gamma_{\text{Be}(3/2^-)}$ [keV]	$\theta_{\text{Be}}^2(3/2^-)[\times 10^{-2}]$	$\Gamma_{\text{Be}(5/2^-)}$ [keV]	$\theta_{\text{Be}}^2(5/2^-)[\times 10^{-2}]$
0^+	27.85	4.21	6	0.31	9	0.52 ($l = 2$)
2^+	28.32	4.68	6	0.30	8	0.23 ($l = 4$)
4^+	29.37	5.73	6	0.14	8	0.10 ($l = 2$)
6^+	30.16	6.51	4	0.32	7	0.25 ($l = 4$)
3^-	31.09	7.45	264	5.37 ($l = 1$)	253	1.84 ($l = 1$)
4^-	31.46	7.82	151	3.02 ($l = 3$)	144	0.92 ($l = 3$)
5^-	31.86	8.22	335	5.81 ($l = 3$)	278	2.21 ($l = 3$)
6^-	32.58	8.95	307	6.33 ($l = 5$)	245	2.10 ($l = 5$)
7^-	33.68	10.0	281	4.87 ($l = 5$)	251	1.51 ($l = 5$)

LC states have very small widths in the ${}^9\text{Be} + {}^9\text{Be}$ channel, which is consistent with the $\alpha + {}^{10}\text{Be} + \alpha$ picture shown in Fig. 3(a). In contrast, the $K^\pi = 3^-$ LC states exhibit large ${}^9\text{Be}$ widths. This strong ${}^9\text{Be} + {}^9\text{Be}$ correlation exhibits that the experimental ${}^9\text{Be} + {}^9\text{Be}$ collision is still a promising way to produce the $K^\pi = 3^-$ LC states if the head-on collision cannot be realized.

To clarify the characteristic ${}^9\text{Be}$ -decay modes, we calculate overlaps between the Brink and AMD wave functions defined as

$$\mathcal{O}(r) = \frac{|\langle \Phi_{\text{BB}}^{K^\pi}(r) | \hat{P}_{KK}^J | \Psi_{\text{AMD}}^\pi \rangle|^2}{|\langle \Phi_{\text{BB}}^{K^\pi}(r) | \hat{P}_{KK}^J | \Phi_{\text{BB}}^{K^\pi}(r) \rangle| |\langle \Psi_{\text{AMD}}^\pi | \hat{P}_{KK}^J | \Psi_{\text{AMD}}^\pi \rangle|}, \quad (7)$$

where \hat{P}_{KK}^J is the angular momentum projection operator. The Brink wave function, $\Phi_{\text{BB}}^{K^\pi}(r)$, is constructed by the linear alignment of two ${}^9\text{Be}$ nuclei, as shown in Fig. 1(a) antiparallel $\Phi_{\text{BB}}^{0^+}(r)$ and (b) parallel $\Phi_{\text{BB}}^{3^-}(r)$ alignments:

$$\Phi_{\text{BB}}^{0^+}(r) = \hat{P}^\pi \mathcal{A} \{ \phi_{\text{Be}}^{jz=3/2}(-r/2) \phi_{\text{Be}}^{jz=-3/2}(r/2) \}, \quad (8)$$

$$\Phi_{\text{BB}}^{3^-}(r) = \hat{P}^\pi \mathcal{A} \{ \phi_{\text{Be}}^{jz=3/2}(-r/2) \phi_{\text{Be}}^{jz=3/2}(r/2) \}. \quad (9)$$

Here, the wave function of ${}^9\text{Be}$ can be described as

$$\phi_{\text{Be}}^{jz} = \mathcal{A} \{ \phi_\alpha \otimes \phi_\alpha \otimes (0p_{3/2}) \}, \quad (10)$$

where $(0p_{3/2})$ is represented by an infinitesimally shifted Gaussian wave packet based on the antisymmetrized quasi-cluster model [39]. Figure 4 shows the calculated overlap as a function of the distance r . The $K^\pi = 3^-$ LC has a large overlap 0.84 with the Brink wave function $\Phi_{\text{BB}}^{3^-}(r = 6.5 \text{ fm})$ shown in Fig. 1(b). In contrast, the $K^\pi = 0^+$ LC has an overlap of 0.52 with $\Phi_{\text{BB}}^{0^+}(r = 5.0 \text{ fm})$ shown in Fig. 1(a). Compared with the $K^\pi = 3^-$ linear chain, the ${}^9\text{Be} + {}^9\text{Be}$ correlation is small in the $K^\pi = 0^+$ LC. The $K^\pi = 3^-$ and $K^\pi = 0^+$ states exhibit different features in the outer region. The $K^\pi = 3^-$ state has a greater overlap in the outer region than that of the $K^\pi = 0^+$ state with the outer peak position. At the present channel radius of 7.0 fm, the overlap of $K^\pi = 3^-$ is one order of magnitude larger than that of $K^\pi = 0^+$, which leads to the much larger ${}^9\text{Be} + {}^9\text{Be}$ decay width. This difference is reflected in the difference in the ${}^9\text{Be}$ -reduced widths listed in Table. III. The $K^\pi = 0^+$ LC has a weak ${}^9\text{Be} + {}^9\text{Be}$ correlation such that the ${}^9\text{Be}$ -reduced widths are small, whereas

the $K^\pi = 3^-$ LC has a strong ${}^9\text{Be} + {}^9\text{Be}$ correlation such that the member states have large ${}^9\text{Be}$ -reduced widths. Therefore, we conclude that the $K = 3^-$ LC states of ${}^{18}\text{O}$ can be observed via ${}^9\text{Be} + {}^9\text{Be}$ resonant scattering shown in Fig. 1(b).

Summary. In summary, we presented the first assessment of the $4\alpha + 2n$ LC configuration in ${}^{18}\text{O}$ using AMD calculation. There are two different 4α LC bands, $K^\pi = 0^+$ and $K^\pi = 3^-$. We predicted their excitation energies, moment of inertia, and α - and ${}^9\text{Be}$ -decay widths. In both bands, the moment of inertia was found to be rather large, which is strong evidence of extreme deformation. The two types of LCs exhibited different decay properties. The $K^\pi = 0^+$ LC states exhibited large decay widths in the $\alpha + {}^{14}\text{C}(\text{LC})$ channel, whereas the $K^\pi = 3^-$ LC states exhibited large decay widths in the ${}^9\text{Be} + {}^9\text{Be}$ channel. To clarify this difference, we calculated overlaps with the ${}^9\text{Be} + {}^9\text{Be}$ Brink wave functions. Consequently, the $K^\pi = 0^+$ LC was found to have a small overlap, whereas the $K^\pi = 3^-$ LC has large overlap, implying that the $K^\pi = 3^-$ LC exhibited

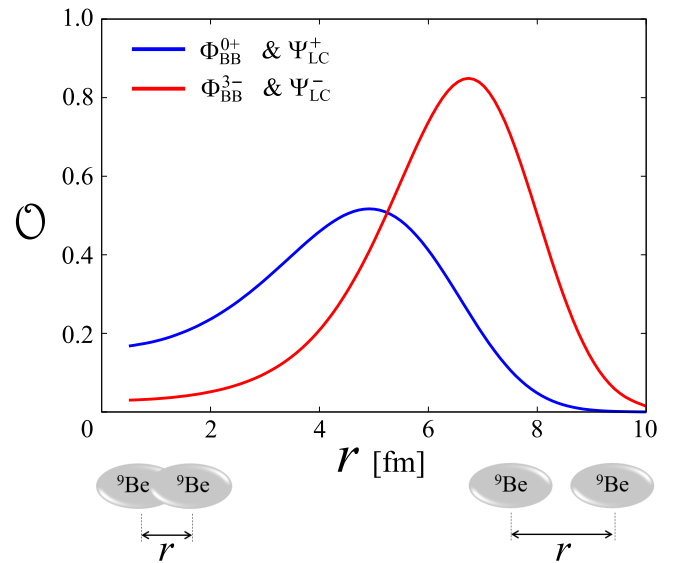


FIG. 4. Calculated overlaps between the ${}^9\text{Be} + {}^9\text{Be}$ Brink and AMD wave functions. Ψ_{LC}^+ and Ψ_{LC}^- correspond to Fig. 3(a) and (b), respectively.

a strong ${}^9\text{Be} + {}^9\text{Be}$ correlation. Therefore, we expect that an LC of ${}^{18}\text{O}$ can be produced by head-on ${}^9\text{Be} + {}^9\text{Be}$ collision. We believe that these are promising characteristics that can be investigated in future experiments to establish the existence of the exotic 4 α LC. Neutron emission channels, which we have not calculated, also have a key role in the experimental search for the LC states. It still remains a challenge for the future.

Acknowledgments. We thank Prof. M. Ito and Dr. H. Yamaguchi for their useful discussions. These calculations have been performed using a supercomputer at the Research Center for Nuclear Physics, Osaka University. The authors acknowledge the support of the collaborative research program 2021 at Hokkaido University. This work has been supported by the JSPS KAKENHI (Grant No. 19K03859).

-
- [1] M. Seya, M. Kohno, and S. Nagata, *Prog. Theor. Phys.* **65**, 204 (1981).
- [2] W. von Oertzen, *Z. Phys. A* **354**, 37 (1996); **357**, 355 (1997).
- [3] Y. Kanada-En'yo, H. Horiuchi, and A. Dote, *Phys. Rev. C* **60**, 064304 (1999).
- [4] M. Freer, J. C. Angélique, L. Axelsson, B. Benoit, U. Bergmann, W. N. Catford, S. P. G. Chappell, N. M. Clarke, N. Curtis, A. D'Arrigo, E. de Goes Brennard, O. Dorvaux, B. R. Fulton, G. Giardina, C. Gregori, S. Grevy, F. Hanappe, G. Kelly, M. Labiche, C. Le Brun, S. Leenhardt, M. Lewitowicz *et al.*, *Phys. Rev. Lett.* **82**, 1383 (1999).
- [5] N. Itagaki and S. Okabe, *Phys. Rev. C* **61**, 044306 (2000).
- [6] M. Ito, N. Itagaki, H. Sakurai, and K. Ikeda, *Phys. Rev. Lett.* **100**, 182502 (2008).
- [7] M. Ito, *Phys. Rev. C* **85**, 044308 (2012).
- [8] N. Itagaki, S. Okabe, K. Ikeda, and I. Tanihata, *Phys. Rev. C* **64**, 014301 (2001).
- [9] N. Furutachi, M. Kimura, A. Dot'è, Y. Kanada-En'yo, and S. Oryu, *Prog. Theor. Phys.* **119**, 403 (2008).
- [10] M. Kimura, *Phys. Rev. C* **75**, 034312 (2007).
- [11] Y. Taniguchi, *Phys. Rev. C* **90**, 054308 (2014).
- [12] M. Freer, J. D. Malcolm, N. L. Achouri, N. I. Ashwood, D. W. Bardayan, S. M. Brown, W. N. Catford, K. A. Chipps, J. Cizewski, N. Curtis, K. L. Jones, T. Munoz-Britton, S. D. Pain, N. Soic, C. Wheldon, G. L. Wilson, and V. A. Ziman, *Phys. Rev. C* **90**, 054324 (2014).
- [13] A. Fritsch, S. Beceiro-Novo, D. Suzuki, W. Mittig, J. J. Kolata, T. Ahn, D. Bazin, F. D. Becchetti, B. Bucher, Z. Chajecki, X. Fang, M. Febraro, A. M. Howard, Y. Kanada-En'yo, W. G. Lynch, A. J. Mitchell, M. Ojaruega, A. M. Rogers, A. Shore, T. Suhara *et al.*, *Phys. Rev. C* **93**, 014321 (2016).
- [14] Z. Y. Tian, Y. L. Ye, Z. H. Li, C. J. Lin, Q. T. Li, Y. C. Ge, J. L. Lou, W. Jiang, J. Li, Z. H. Yang, J. Feng, P. J. Li, J. Chen, Q. Liu, H. L. Zang, B. Yang, Y. Zhang, Z. Q. Chen, Y. Liu, X. H. Sun *et al.*, *Chin. Phys. C* **40**, 111001 (2016).
- [15] H. Yamaguchi, D. Kahl, S. Hayakawa, Y. Sakaguchi, K. Abe, T. Nakao, T. Suhara, N. Iwasa, A. Kim, D. H. Kim, S. M. Cha, M. S. Kwag, J. H. Lee, E. J. Lee, K. Y. Chae, Y. Wakabayashi, N. Imai, N. Kitamura, P. Lee, J. Y. Moon *et al.*, *Phys. Lett. B* **766**, 11 (2017).
- [16] J. Li, Y. L. Ye, Z. H. Li, C. J. Lin, Q. T. Li, Y. C. Ge, J. L. Lou, Z. Y. Tian, W. Jiang, Z. H. Yang, J. Feng, P. J. Li, J. Chen, Q. Liu, H. L. Zang, B. Yang, Y. Zhang, Z. Q. Chen, Y. Liu, X. H. Sun *et al.*, *Phys. Rev. C* **95**, 021303(R) (2017).
- [17] T. Suhara and Y. Kanada-En'yo, *Phys. Rev. C* **82**, 044301 (2010).
- [18] J.-P. Ebran, E. Khan, T. Nikšić, and D. Vretenar, *Phys. Rev. C* **90**, 054329 (2014).
- [19] T. Baba and M. Kimura, *Phys. Rev. C* **94**, 044303 (2016).
- [20] T. Baba and M. Kimura, *Phys. Rev. C* **95**, 064318 (2017).
- [21] Y. Kanada-En'yo and K. Ogata, *Phys. Rev. C* **101**, 014317 (2020).
- [22] Z. X. Ren, P. W. Zhao, and J. Meng, *Phys. Lett. B* **801**, 135194 (2020).
- [23] T. Baba and M. Kimura, *Phys. Rev. C* **97**, 054315 (2018).
- [24] Y. Liu, Y. L. Ye, J. L. Lou, X. F. Yang, T. Baba, M. Kimura, B. Yang, Z. H. Li, Q. T. Li, J. Y. Xu, Y. C. Ge, H. Hua, J. S. Wang, Y. Y. Yang, P. Ma, Z. Bai, Q. Hu, W. Liu, K. Ma, L. C. Tao *et al.*, *Phys. Rev. Lett.* **124**, 192501 (2020).
- [25] T. Baba, Y. Liu, J. X. Han, and Y. L. Ye, *Phys. Rev. C* **102**, 041302(R) (2020).
- [26] Y. Suzuki, H. Horiuchi, and K. Ikeda, *Prog. Theor. Phys.* **47**, 5 (1972).
- [27] T. Ichikawa, J. A. Maruhn, N. Itagaki, and S. Ohkubo, *Phys. Rev. Lett.* **107**, 112501 (2011).
- [28] T. Suhara, Y. Funaki, B. Zhou, H. Horiuchi, and A. Tohsaki, *Phys. Rev. Lett.* **112**, 062501 (2014).
- [29] J. M. Yao, N. Itagaki, and J. Meng, *Phys. Rev. C* **90**, 054307 (2014).
- [30] Y. Suzuki and W. Horiuchi, *Phys. Rev. C* **95**, 044320 (2017).
- [31] T. Inakura and S. Mizutori, *Phys. Rev. C* **98**, 044312 (2018).
- [32] J. F. Berger, M. Girod, and D. Gogny, *Comput. Phys. Commun.* **63**, 365 (1991).
- [33] M. Kimura, *Phys. Rev. C* **69**, 044319 (2004).
- [34] Y. Kanada-En'yo and H. Horiuchi, *Prog. Theor. Phys.* **93**, 115 (1995).
- [35] D. L. Hill and J. A. Wheeler, *Phys. Rev.* **89**, 1102 (1953).
- [36] T. Baba and M. Kimura, *Phys. Rev. C* **100**, 064311 (2019).
- [37] D. R. Tilley, J. H. Kelley, J. L. Godwin, D. J. Millener, J. E. Purcell, C. G. Sheu, and H. R. Weller, *Nucl. Phys. A* **745**, 155 (2004).
- [38] Y. Funaki, H. Horiuchi, and A. Tohsaki, *Prog. Part. Nucl. Phys.* **82**, 78 (2015).
- [39] T. Suhara, N. Itagaki, J. Cseh, and M. Płoszajczak, *Phys. Rev. C* **87**, 054334 (2013).